


# Energy-saving potential of cool roofs at the urban scale: A case study of Xiamen city

Chengcheng Song<sup>a</sup>, Yixing Chen<sup>a,b,\*</sup> 

<sup>a</sup> College of Civil Engineering, Hunan University, Changsha 410082, China

<sup>b</sup> Key Laboratory of Building Safety and Energy Efficiency of Ministry of Education, Hunan University, Changsha 410082, China

## ARTICLE INFO

### Keywords:

Cool roof  
Urban building energy modeling  
EnergyPlus  
AutoBPS  
Building retrofits

## ABSTRACT

Urban-scale energy modeling of cool roof retrofits requires detailed knowledge of rooftop. This study developed a high-resolution Urban Building Energy Modeling (UBEM) framework that integrates roof reflectance data for Xiamen City, China. First, building types were classified using Geographic Information System (GIS) and machine learning techniques. Then, historical satellite imagery was analyzed to estimate the building year of each building. Roof color and reflectance were subsequently evaluated using Sentinel-2 and high-resolution imagery. This process resulted in the creation of a multi-source geospatial dataset comprising 37,132 buildings in Xiamen. A physics-based UBEM was then constructed using AutoBPS for 31,608 buildings to simulate energy performance under three scenarios: baseline, measured reflectance, and cool roof retrofit. Compared to the default reflectance value of 20 %, actual roof reflectance in Xiamen reduced energy consumption by 1.8 % (0.94 GWh). Furthermore, three types of cool roof technologies, spray coatings, membranes, and metal roofs, achieved annual energy savings of 4.42 % (2.32 GWh), 3.58% (1.88 GWh), and 2.27 % (1.19 GWh), respectively. Their corresponding peak-load reductions were 10.7 %, 8.97 %, and 5.5 %. Among the 31,608 buildings modelled, 3790 buildings (approximately 12 %) met the economic feasibility criterion of a payback period under 10 years. Of these, 1298 buildings were more suitable for membrane application and 2492 for spray coating. Over their life cycle, these buildings would require an initial investment of 35.3 million CNY and maintenance costs of 39.3 million CNY, yielding electricity savings of 151.67 GWh, equivalent to 89.6 million CNY, and resulting in net savings of 15.0 million CNY.

## 1. Introduction

Urban building energy consumption and carbon emissions constitute a significant portion of global energy use and carbon output. To address this issue, governments worldwide are actively implementing energy-saving measures. In addition to adopting higher energy efficiency standards for new constructions, retrofitting existing buildings is a crucial component. For policymakers, it is essential to evaluate the effectiveness of various retrofitting strategies through modeling before implementation.

The roof of a building is a major building envelope component that receives significant solar radiation [1]. Heat transfer through the roof can account for more than 40 % of top-floor energy consumption and 5–10 % of a building's total cooling electricity usage [2]. To mitigate this, researchers often employ cool roofs and green roofs [3] to reduce radiation absorption. Cool roofs use high-reflectivity and high-

emissivity materials to lower heat absorption, while green roofs provide insulation, regulate stormwater runoff, and offer ecological benefits through vegetation coverage. However, these two strategies differ in applicability, cost, and climate adaptability. Jia et al. [4] evaluated both cool roofs and green roofs under current and future scenarios across six global cities, and projected that by 2100, and the Heating, Ventilation, and Air Conditioning (HVAC) energy consumption would be reduced by 65.51 % and 71.72 %, respectively. He et al. [5] found that in Shanghai, green roofs reduced the cooling and heating loads of the top floor by 3.6 % and 6.2 %, respectively, while cool roofs reduced the cooling load by 3.6 % but increased the heating load by 10.4 %. These results suggest that in Shanghai and similarly warmer regions, cool roofs offer energy-saving potential comparable to green roofs.

Assessing the impact of cool roofs on energy consumption at an urban scale requires a fundamental understanding of urban building energy use [6]. Urban Building Energy Modeling (UBEM) is a technique

\* Corresponding author at: College of Civil Engineering, Hunan University, Changsha 410082, China.

E-mail address: [yixingchen@hnu.edu.cn](mailto:yixingchen@hnu.edu.cn) (Y. Chen).

<https://doi.org/10.1016/j.enbuild.2025.116034>

Received 28 April 2025; Received in revised form 2 June 2025; Accepted 13 June 2025

Available online 14 June 2025

0378-7788/© 2025 Elsevier B.V. All rights are reserved, including those for text and data mining, AI training, and similar technologies.

designed for this purpose, employing various approaches such as top-down and bottom-up models [7]. Among bottom-up methods, physics-based simulations and machine learning models are commonly used [8]. Retrofitting often involves new technologies and materials, which lack sufficient historical data. As such, machine learning and top-down methods may struggle to evaluate their effectiveness accurately. 83 % of retrofit studies utilize physics-based simulation tools like EnergyPlus and TRNSYS [9]. Bottom-up UBEEM calculates energy consumption by simulating physical heat transfer and equipment energy interactions at the individual building level, then aggregates results to the urban scale [10]. This high-resolution approach offers significant flexibility in analyzing the impact of retrofitting strategies across regions. Additionally, due to variations in urban morphology, building compositions, and climate conditions, the same retrofitting measures may yield different outcomes in different cities. For example, Ang et al. (2023) observed that identical retrofit strategies led to significant energy savings in some cities but increased energy consumption in others, underscoring the necessity of context-specific solutions.

The quality of UBEEM outputs is intrinsically linked to the quality of its inputs. Developing a bottom-up UBEEM requires comprehensive data on all buildings in a region, presenting one of its biggest challenges [7], particularly in parameter calibration. Directly obtaining detailed building envelope data for each building is very hard, researchers typically rely on GIS tools to derive building year and type and use archetype modeling to estimate energy consumption [11]. Deng et al. [12] used GIS to classify buildings by correlating POI data with building attributes. Song et al. [13] integrated multi-source data for 539,119 buildings in Shanghai and applied GIS and machine learning to determine building year and type, subsequently constructing UBEEM using AutoBPS. Similarly, Sun et al. [14] employed GIS to estimate building energy consumption and age in Wellington, New Zealand. Biljecki et al. [15] utilized 3D GIS data to estimate building year.

In addition to non-geometric parameters such as building year and type, exterior parameters have also garnered attention. Wang et al. [16] proposed a systematic method to obtain footprint, height, and window-to-wall ratio data. Chen et al. [17] employed natural language processing to extract building types in Beijing using points of interest. Lu et al. [18] analyzed structural, spectral, and spatial characteristics in satellite imagery, leveraging support vector machines and LiDAR data to classify buildings into single-family, multi-family, and non-residential categories with 70 % accuracy. Szcześniak et al. [19] extracted window-to-wall ratios for over 1000 buildings in Manhattan using street view images to calibrate UBEEM.

Despite the importance of roofs in UBEEM energy modeling [20], research combining roof retrofits with UBEEM remains limited. Wang et al. [21] investigated green roofs in Xiamen, using GIS to classify buildings and prototype modeling to assess their impact, concluding that green roofs could achieve 1.62–1.83 % energy savings and 1.10–1.63 % peak load reduction citywide. Jia et al. [4] reported that cool roofs reduced cooling energy consumption by 67.18–86.70 % on average across six cities, while green roofs achieved reductions of 63.38–83.21 %. Adilkanova [22] found that green roofs in Seoul delivered energy savings of up to 0.64 kWh/m<sup>2</sup> (7.7 %). Hosseini et al. [23] estimated that cool roofs in four cold-climate North American cities reduced peak power demand by 1.9–5.4 W/m<sup>2</sup>. Garshabi et al. [24] researched buildings in Sydney, Australia, showed cool roofs reduced energy consumption by 29.8–72.4 % in residential buildings, 22.4–62.5 % in office buildings, and 13.2–29.1 % in commercial buildings. The effectiveness of cool roofs retrofit differs significantly across various cities. Building characteristics, such as the roof's original reflectance, envelope properties, etc., critically influence how cool roof retrofits affect energy consumption. Therefore, the performance of cool roof retrofits should be evaluated using data that reflect the specific urban and building contexts of each city. Currently, roof type detection is not integrated into UBEEM well. Lalwani et al. [25] identified cool roofs in India but did not evaluate their impact. Park et al. [26] used CNN to detect green and cool

roofs across eight cities, estimating 14 % and 28 % energy savings, respectively. Qian et al. [27] employed a multitask deep learning network to classify roof types in Shanghai. Trevisiol [28] used very high-resolution satellite imagery to detect roof materials in Bologna, Italy, achieving 91 % accuracy. These literatures indicate that roof detection methods are relatively mature and can serve as a foundation for UBEEM. Actual rooftop parameters have not been sufficiently explored in current bottom-up UBEEM studies, and a dedicated evaluation framework for cool roofs within UBEEM remains lacking. Roof-related parameters are often assessed using default values. However, relying on default assumptions without considering predicted rooftop conditions may introduce notable biases, particularly in cities with substantial cool roof coverage. Moreover, the method used to aggregate simulation results requires improvement, as shading effects from surrounding buildings can significantly influence the outcomes. A building-by-building approach would provide more accurate results. To address this gap, this study will develop a UBEEM framework that incorporates the specific roof characteristics of Xiamen. The objectives of this study are as follows: (1) To investigate the actual distribution of rooftop parameters in Xiamen; (2) To develop a UBEEM for Xiamen that incorporates both real rooftop characteristics and surrounding shading conditions, in order to accurately capture the impact of cool roofs; (3) To quantify the energy-saving potential of various cool roof retrofit scenarios in Xiamen based on the developed UBEEM.

## 2. Methodology

Fig. 1 presents the methodological framework developed for the construction of a comprehensive Xiamen building dataset and an UBEEM for Xiamen city.

This UBEEM framework employs a multi-stage process, integrating multi-source data to derive fundamental building geometry and type (Part I). This process involves the utilization of inputs such as points of interest (POIs), building footprints, areas of interest (AOIs), and satellite imagery. Data fusion, GIS analysis, and machine learning techniques are employed to ascertain building footprints, height/stories, and building types. Part II addresses the temporal dimension by estimating building year through GIS analysis and change detection applied to community datasets and historical satellite imagery. Part III characterizes building roof properties, specifically reflectance and color, through the analysis of very high-resolution (VHR) and Sentinel-2 satellite imagery. The outputs from Parts I, II, and III collectively provide detailed building dataset in Xiamen city, formatted as GeoJSON. Part IV is to translate this GeoJSON into EnergyPlus models using the AutoBPS (Automated Building Performance Simulation) tool. Subsequently, city-scale building energy modeling is performed in Part V to model building energy consumption across Xiamen city. The application of cool roof technology as a building energy efficiency measure is then evaluated using the UBEEM. The final results compare energy consumption under baseline roof properties, measured reflectance, and cool roof scenarios.

### 2.1. Introduction to the case study area

This study focuses on the center part Xiamen city as the research area as shown in Fig. 2. Xiamen city is situated within Fujian Province, in the southeastern coastal region of China. Geographically, the island is located approximately between 24°26' and 24°32' north latitude, and 118°04' and 118°11' east longitude. Covering an area of approximately 158 square kilometers, the island's topography is predominantly hilly. Administratively, Xiamen city encompasses the Siming and Huli districts and has a population of approximately 1.2 million residents. The climate of Xiamen is characterized as a subtropical maritime monsoon climate, with an average annual temperature of around 21 °C and an average annual precipitation of approximately 1200 mm, with the majority of rainfall occurring between May and August.

This study builds upon previous research by expanding the scope of

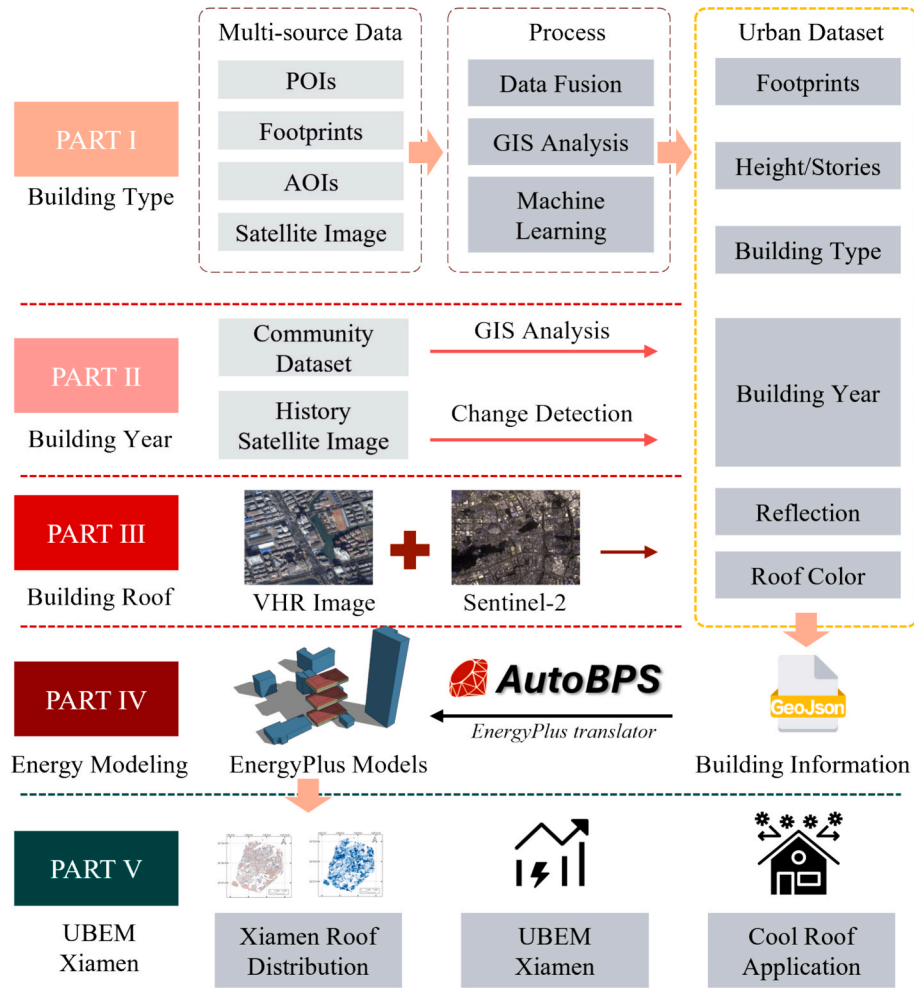


Fig. 1. Workflow of this study.

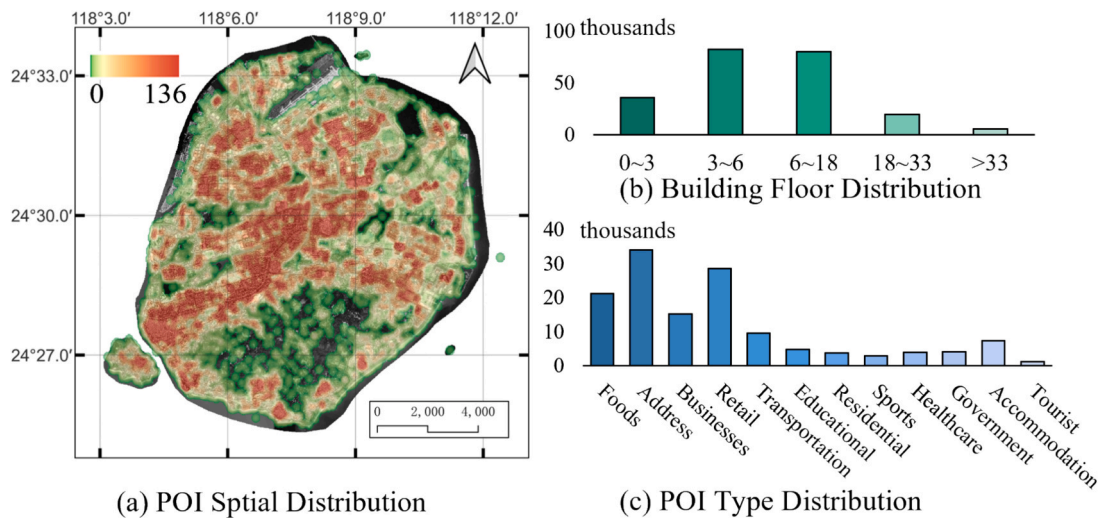


Fig. 2. Introduction of Xiamen.

analysis. GIS data from relevant sources for the target area are first acquired, including POIs, AOIs, land use data, building footprints, and specific neighborhood information. POIs are defined as distinct locations with functional significance, such as buildings or landmarks. Footprints represent the geometric boundaries of individual buildings or structures.

AOIs encompass broader geographic regions of study, often including multiple footprints or POIs, providing a foundational framework for spatial analysis and classification.

As illustrated in Fig. 2(a), the red areas indicate a higher concentration of POIs, suggesting greater activity in these areas. Fig. 2(b)

reveals the distribution of building floor counts, suggesting a prevalence of low-rise to mid-rise structures in Xiamen, with a significant proportion of buildings having between 3 and 18 floors. Furthermore, Fig. 2(c) presents the distribution of various POI types.

## 2.2. Data preparation

### 2.2.1. GIS data

The data incorporated in this study were derived from a multi-source geospatial database, encompassing Baidu Map, Amap (Gaode Map), Google Map, and OpenStreetMap. In accordance with the methodology of Song et al. [13], these datasets underwent a rigorous integration and calibration process to ensure inter-dataset consistency. The resulting harmonized data were subsequently aggregated, incorporating building type and building year attributes, to form the foundational dataset. For the Xiamen region, the integrated and calibrated dataset comprises 3,731 AOIs, 224,586 POIs, and 37,132 buildings. Given that the acquired GIS data had been subjected to manual verification by a mapping company, exhibiting relatively high accuracy in attributes such as building height, this study employed building footprints with height information, registered against satellite imagery, rather than direct rooftop outline extraction. This approach was adopted to preserve detailed architectural features and to mitigate potential inaccuracies in rooftop delineation resulting from tile boundary discontinuities.

### 2.2.2. Multi-channel imagery

Previous studies often relied on default parameters for prototype building roof types, an approach that oversimplifies the heterogeneity of real-world urban environments. To address this limitation, the current research endeavors to contextualize prototype building roof reflectivity by leveraging high-spatial-resolution satellite imagery for improved accuracy. While multispectral satellite imagery, such as that acquired by Sentinel-2, offers valuable spectral information across visible to near-infrared wavelengths suitable for surface reflectance calculation, its spatial resolution (10–60 m) proves insufficient for detailed identification and analysis of complex and varied urban roof structures. In contrast, VHR imagery provided by Google satellites, boasting a spatial resolution of 0.25 m, enables the clear delineation of fine-scale architectural features, facilitating precise roof extraction and boundary identification. This study employs the Python programming language in conjunction with the Google Earth Engine (GEE) platform to systematically acquire and process both Sentinel-2 Multispectral Instrument and 0.25 m VHR imagery from Google satellites for the accurate computation of building roof reflectivity. Specifically, the “Sentinel-2A” dataset, provided by the European Space Agency and encompassing 13 spectral bands with a 5-day revisit frequency, was utilized. This dataset undergoes rigorous pre-processing, including radiometric calibration, atmospheric correction, and geometric rectification, ensuring spectral and spatial consistency and accuracy. The study area is geographically constrained to a rectangular region spanning 118.05° to 118.20° East longitude and 24.40° to 24.58° North latitude. Temporal analysis was conducted across two distinct periods: May 1st to September 30th, 2024, to capture summer reflectivity characteristics, and December 1st, 2024, to February 1st, 2025, to represent winter reflectivity.

To minimize the influence of varying weather conditions on reflectance accuracy, surface reflectance data from the Google Earth Engine platform were employed. These datasets had undergone atmospheric and orthorectification corrections to ensure geometric and radiometric consistency. Image compositing was performed using pixels with low cloud coverage ( $QA60 \leq 8\%$ ), and only scenes meeting this criterion were included. A mean compositing method was adopted to mitigate the effects of short-term weather fluctuations and illumination inconsistencies. Reflectance values were extracted across two distinct time periods, May to September 2024 (summer) and December 2024 to February 2025 (winter), to capture seasonal variability. Subsequently, an average of the summer and winter reflectance values was calculated

to obtain a single representative result. This temporally averaged value is considered robust, as it integrates multi-seasonal surface conditions while reducing noise introduced by transient atmospheric effects.

As illustrated in the Fig. 3, the 13 spectral bands of Sentinel-2A span the visible to shortwave infrared range, ordered by increasing wavelength. Specifically, B1 (443 nm, Coastal aerosol, 60 m) is dedicated to aerosol monitoring and coastal water analysis. B2, B3, and B4 (10 m) constitute the visible light spectrum, facilitating surface color identification. The red-edge bands, B5, B6, and B7 (20 m), are specialized for retrieving vegetation biochemical parameters. Bands B8 (near-infrared, 10 m) and B8A (narrow near-infrared, 20 m) serve in vegetation classification and water body delineation. B9 (water vapor, 60 m) supports atmospheric correction procedures, while B10 (cirrus, 60 m) is employed for cloud screening. The shortwave infrared bands, B11 and B12 (20 m), exhibit sensitivity to surface moisture and material composition. The blue, green, and red bands (B2–B4) effectively represent surface color and vegetation cover within the visible spectrum. The near-infrared band (B8) is sensitive to vegetation health and enables discrimination between artificial structures and natural surfaces. The shortwave infrared bands (B11–B12) can penetrate atmospheric water vapor, allowing for the identification of spectral signatures of diverse roofing materials, such as metal and asphalt. These bands were selected to optimize the balance between spectral resolution, atmospheric correction robustness, and sensitivity to roof material heterogeneity, thereby supporting urban land cover classification and reflectance modeling.

In the process of aligning VHR and multispectral imagery, some alignment issues were encountered, necessitating the conversion of footprints to raster format. Additionally, this research acquired 0.25-meter resolution VHR imagery data from Google, encompassing the red, green, and blue (RGB) visible bands. To ensure spatial consistency between the VHR imagery and the Sentinel-2 multispectral data, precise registration was performed on the VHR imagery. This involved feature matching using the Scale-Invariant Feature Transform algorithm, and affine transformation methods were employed during the image pre-processing stage to execute geometric correction, thereby guaranteeing spatial alignment between the two datasets.

## 2.3. Building type

As shown in the Fig. 4, the classification of building categories in this paper relies on the systematic integration and intelligent analysis of multi-source open data. The study constructs a building attribute database covering the entire Xiamen by fusing building footprint data, high-

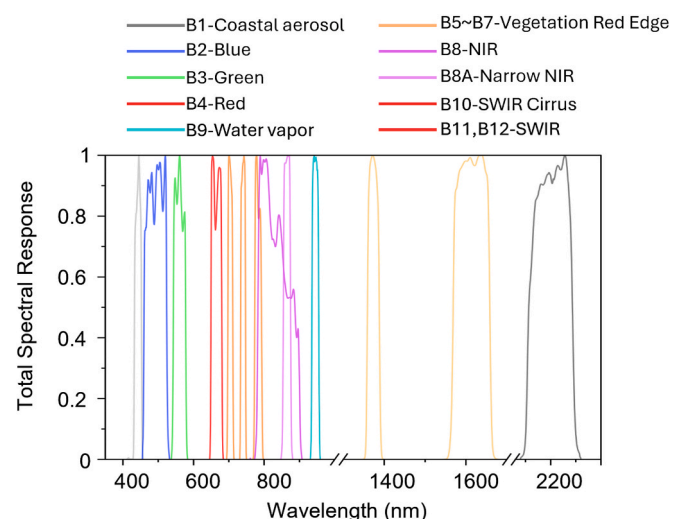


Fig. 3. Spectral response for the Sentinel-2A multispectral instrument sensor.



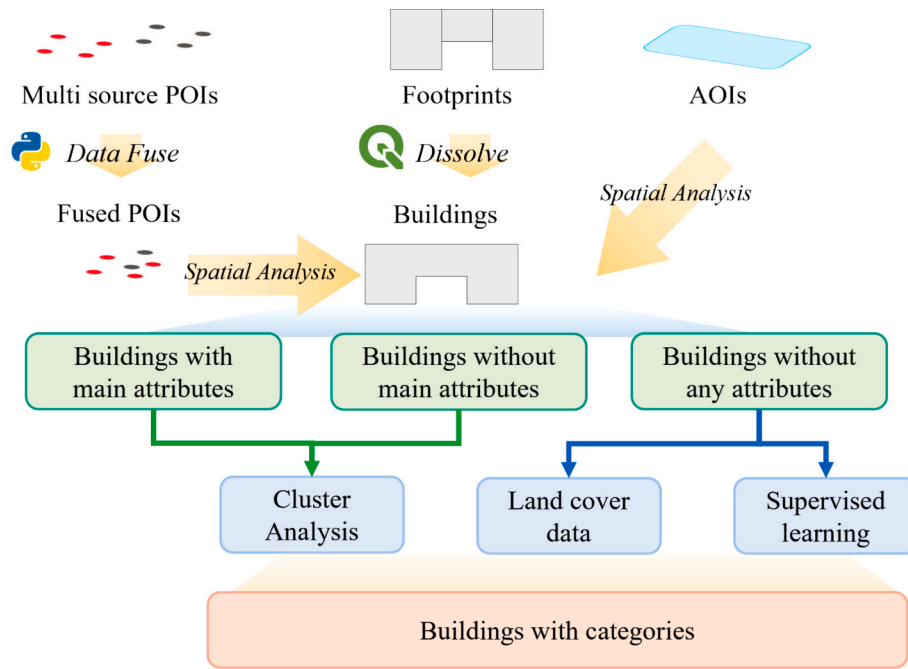


Fig. 4. Methodological framework of building type detection.

resolution satellite imagery, POIs, and land cover datasets. Firstly, POI attributes are associated with building geometry data (such as area, height, shape index) based on a spatial matching algorithm. Data fusion and redundancy elimination are performed using buffer analysis and natural language processing techniques to initially identify major functional types such as residential, commercial, and educational. For buildings lacking POI and AOI information indicating major functional types, K-means clustering is employed to group them based on their POI distribution patterns and morphological characteristics. Finally, land use data is utilized to supplement the information. Detailed methodology can be found in Song et al. [13]

#### 2.4. Building year

In this study, the division of building year primarily relies on two methods as shown in the Fig. 5. The first method involves cross-referencing historical imagery. The second method utilizes data from real estate websites, which offer extensive information about the

locations of residential communities and their corresponding building years. Additionally, the AOI data predominantly focuses on residential communities. Data from real estate websites often originate from information uploaded by property developers, making this method capable of yielding more accurate, specific, and authentic data. This paper obtained specific information for 2033 residential communities on Xiamen city from real estate websites such as Lianjia and Anjuke. Considering that such data is commercially maintained in real time by property sales platforms, its accuracy and timeliness are significantly higher than those of open datasets or machine learning predictions. Therefore, we directly used this data to override the building year estimates obtained from machine learning. By integrating this information with the AOI data, the construction years of 9210 buildings were updated. Among these, 914 buildings had a discrepancy of more than five years compared to the machine learning predictions, indicating that the building year prediction accuracy in this study exceeds 90 %.

Since the modeling parameters of buildings are mainly related to mandatory standards issued by the area, this paper references JGJ 134–2001 and JGJ 134–2010 for residential buildings, dividing them into pre-2001, 2001–2010, and post-2010 categories, respectively. Commercial buildings are divided into pre-2005, 2005–2015, and post-2015 based on the standards GB 50189–2005 and GB 50189–2015, the referenced codes, JGJ 134 (specifically for residential buildings) and GB 50189 (Design standard for energy efficiency of public buildings), are mandatory national standards in China. This means that building construction projects within their scope must comply with the requirements set forth in these documents. These standards dictate various design and performance criteria, which have been updated over time (as indicated by the different publication years). While they are national standards, they often contain specific provisions or are implemented alongside regional regulations that account for variations in climate zones and local conditions across China. The paper uses the effective dates of these different versions to categorize buildings based on the regulations they were likely designed and built under.

In our previous research methodologies, building data were typically downloaded from these temporal intervals, and machine learning techniques were employed for the detection of building changes. While this approach has demonstrated efficacy in rapidly expanding urban areas, its performance in Xiamen is suboptimal. This discrepancy is

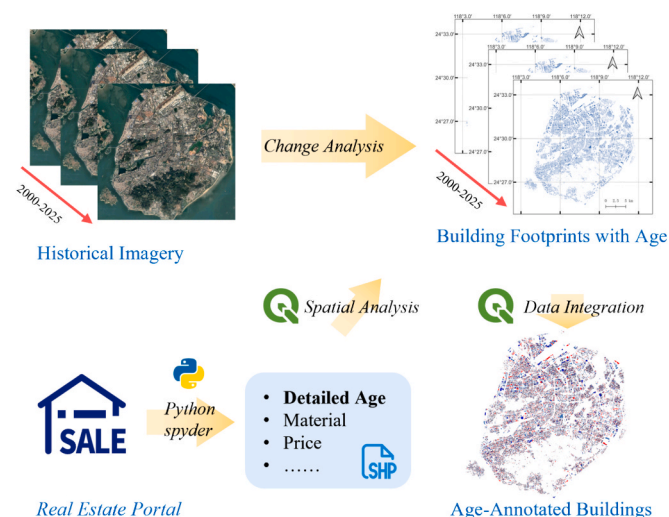


Fig. 5. Methodological framework of building year Detection.

attributed to the substantial prevalence of roof renovation and reconstruction activities within Xiamen, as illustrated in the Fig. 6. Consequently, the accurate determination of building year through sole reliance on change detection proves to be challenging.

This paper introduces a novel approach (Fig. 7) that, unlike object detection algorithms like Mask R-CNN, leverages multi-year historical imagery and roof vector data. This method delineates building footprints across time, creating a temporal sequence of building extents. A CNN classification model then determines building presence within these footprints. Concurrently, significant roof color changes are identified. A transition from 'non-building' to 'building' indicates new construction; substantial color change without new construction signifies roof renovation; and a 'building' to 'non-building' to 'building' sequence implies reconstruction, with the latter date assigned as the construction year.

To address the challenges of scale diversity, shape complexity, and background interference in Xiamen's historical satellite imagery, we employed transfer learning and the lightweight MobileNet V2 architecture (with depthwise separable convolutions and inverted residual modules for efficient feature extraction – 75 % fewer parameters than ResNet-50). This approach improved generalization for building features. The dataset comprised 678 building and 247 non-building images (bare land, grassland, construction sites, etc.). Preprocessing included standardization using ImageNet statistics (mean [0.485, 0.456, 0.406], std [0.229, 0.224, 0.225]) for stability and faster convergence. Data augmentation, including horizontal/vertical flips, brightness/contrast adjustments, and cloud and shadow simulation, expanded the dataset to 3700 images, simulating real-world variations and improving model robustness. The data was split 60:20:20 for training, validation, and testing.

During the model training process, Focal Loss was used as the loss function. Focal Loss dynamically adjusts the contribution of each sample to the total loss, enabling the model to focus more on hard-to-classify samples during training. Its formulation is presented in Eq. (1).

$$FL(p_t) = -\alpha(1 - p_t)^\gamma \log(p_t) \quad (1)$$

Where  $p_t$  is the probability of belonging to the positive class, the parameter  $\alpha$  is used to balance the importance of positive and negative samples, and the parameter  $\gamma$  controls the loss weight difference between easy and hard samples. This mechanism is particularly suitable for handling the class imbalance problem between building and non-building areas in satellite imagery, effectively improving the model's ability to identify complex regions such as building boundaries. After testing, we finally determined  $\alpha = 0.25$ , and  $\gamma = 2$ . The training adopted a two-stage transfer learning strategy. First, the backbone network was frozen for feature adaptation training, and subsequently, the entire network was unfrozen for end-to-end fine-tuning. A dynamic learning rate adjustment mechanism (initial value 0.001, decay coefficient 0.5) combined with an early stopping rule (terminating training if the validation loss plateaus for 5 epochs) enabled rapid model convergence within the 20th training epoch.

In machine learning model evaluation, the meanings of common metrics are as follows: Loss measures the error between predictions and true labels (lower values are better); Accuracy represents the proportion of correctly predicted samples (easily affected by class imbalance); Precision reflects the proportion of actual positive samples among those predicted as positive, Recall represents the proportion of actual positive samples that were correctly predicted, and the F1-score is the harmonic mean of Precision and Recall, comprehensively evaluating the classification quality (especially suitable for scenarios with class imbalance). The results of this model are shown in the Table 1.

Table 1 indicates that although the model may exhibit some overfitting, it can perform the task well and achieve a good balance between the two outcomes (generally, an F1 score greater than 0.85 is considered qualified). We believe that this method can more effectively detect building construction time, reconstruction time, and roof renovation time, providing results with high temporal resolution. Furthermore, the computational efficiency of this classification method is significantly higher than that of segmentation algorithms, reducing the processing time from days to hours. The required clarity of satellite imagery for classification is also greatly reduced, which means the data download burden will be significantly lower. For this task, the download volume was reduced from 250 GB to 10 GB, and the computation time was reduced from 30 h (6 h \* 5 tasks) to 20 min (1 min \* 20 tasks).

## 2.5. Building rooftop reflection

In multispectral remote sensing applications, the development of composite spectral indices through weighted band combinations is a common approach to enhance the discriminative capacity of specific surface features. This technique requires rigorous spectral analysis to determine optimal weighting coefficients that maximize inter-class separability while minimizing intra-class variability. The method adopted in this study was proposed and experimentally validated by Bonafoni and Sekertekin [29], and is considered effective for evaluating urban albedo. The calculation of the integrated reflectance is shown in Eq. (2).

$$\alpha = \sum_{B=1}^N \rho_B \cdot w_B \quad (2)$$

where  $\rho_B$  is the surface reflectance for a specific band B, and  $w_B$  is the weighting coefficient computed as Eq. (3)

$$w_B = \frac{\int_{L_B}^{U_B} R_{sl} \cdot d\lambda}{\int_{0.3}^3 R_{sl} \cdot d\lambda} \quad (3)$$

where  $R_{sl}$  is the at-surface spectral solar radiation at wavelength  $\lambda$  ( $\mu\text{m}$ ), and  $U_B, L_B$  are the upper and lower wavelength for band B.  $w_B$  represents the weighted fraction of solar radiation within the spectral range of band B. Integration limits were set to 0.3–3  $\mu\text{m}$ , covering nearly all at-surface

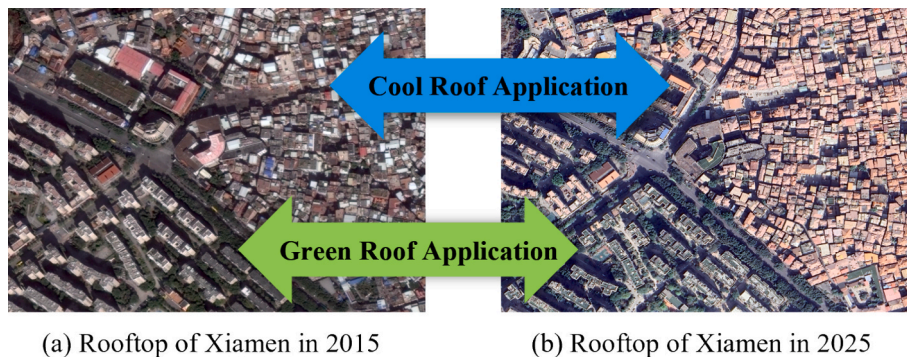


Fig. 6. Rooftop renovations in Xiamen in recent years.

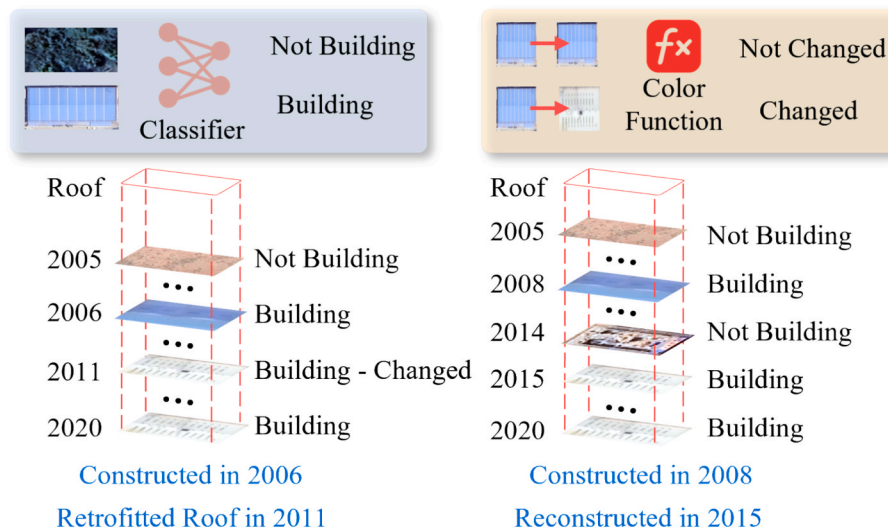


Fig. 7. Roof change detection method framework.

**Table 1**  
Confusion matrix for building detection model.

Metric	Loss	Accuracy	F1	Precision	Recall
Training	0.0007	0.9952	0.9968	0.9989	0.9947
Validation	0.0368	0.9551	0.9758	0.9758	0.9758
Test	—	0.9467	0.9715	0.9642	0.9788

solar radiation, the specific parameters used and the corresponding calculated values are presented in Table 2.

As shown in Table 2, Near-infrared (B8) has the highest weight (34.17 %) due to its ability to effectively distinguish building rooftops and has an excellent signal-to-noise ratio. Blue light (B2) holds the second highest weight (22.66 %) and is used to enhance the high reflection characteristics of metal roofs. The weights of red light (B4) and green light (B3) reflect their sensitivity to common roof colors (such as red tiles and green coatings). Shortwave infrared (B11–B12) has a lower weight because it is easily affected by cloud and aerosol interference, but it can help identify heat-absorbing materials such as asphalt.

## 2.6. Building energy model generation

The modeling process consists of two main components. The first involves data input, accomplished through Python scripts. Following the calculation of surface reflectance, shading effects from surrounding buildings are assessed.

To accurately reflect shading conditions while reducing computational complexity, we first screened for potential shadow-casting buildings that could obstruct the target building. A building is identified as a shading obstacle if its shadow affects the target building for more than 80 % of the time between 8:00 AM and 6:00 PM on the winter solstice, corresponding to a solar elevation angle of approximately

**Table 2**  
MSI Spectral Bands Information.

Channels	Central wavelength (μm)	Bandwidth (μm)	$U_B$ and $L_B$ (μm)	$w_B$
B2	0.492	0.066	0.3–0.533	0.2266
B3	0.559	0.036	0.533–0.614	0.1236
B4	0.665	0.031	0.614–0.730	0.1573
B8	0.833	0.106	0.730–1.226	0.3417
B11	1.612	0.092	1.226–1.880	0.117
B12	2.194	0.18	1.880–3.00	0.0338

18.6°. During this process, no geometric simplifications were applied to the selected shadows, to faithfully represent shading conditions in areas with complex building layouts.

This filtering method reduces the number of shading surfaces and generates the shading geometry, as illustrated in Fig. 8. To further improve computational efficiency, identical floors with similar thermal conditions are represented by a single representative floor, as implemented in AutoBPS. The filtered model is then imported into CityEL [30], where the geometry of the EnergyPlus model is adjusted based on the building's footprint dimensions: length, width, height, and number of floors. The final model, incorporating a uniform window-to-wall ratio of 0.4, is used as input for energy simulation.

For non-geometric parameters, the classification is based on mandatory national building regulations, categorizing buildings by building year and building type. Xiamen is classified as a hot summer and warm winter region according to these regulations. Residential buildings are divided into three temporal categories based on Standards JGJ 134–2001 and JGJ 134–2010: pre-2001, 2001–2010, and post-2010. Commercial buildings follow a similar tripartite classification according to Standards GB 50189–2005 and GB 50189–2015, segmented as pre-2005, 2005–2015, and post-2015. For mixed-use buildings, relevant regulatory criteria are applied to each functional component individually. In cases where data are not explicitly provided in the standards, estimations were made based on the building year. The final parameters used are presented in Table 3.

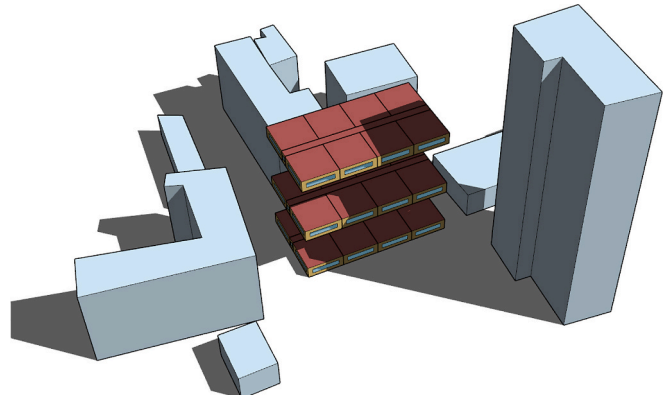


Fig. 8. EnergyPlus model of the building, including surrounding buildings.

**Table 3**  
EnergyPlus model settings of each prototype building parts of Xiamen.

Parameters	Residential part			Commercial part		
	Pre-2001	2001–2010	Post-2010	Pre-2005	2006–2014	Post-2015
Exterior wall U-value(W/(m <sup>2</sup> *K))	2.47	2	1.5	1.8	0.8	0.6
Roof U-value (W/(m <sup>2</sup> *K))	1.8	1	0.9	1.55	0.7	0.5
Window U-value (W/(m <sup>2</sup> *K))	5.84	4.09	4.09	6.4	3.5	2.5
Window SHGC	0.62	0.362	0.362	0.69	0.4	0.3
Lighting power density (W/m <sup>2</sup> )	5.5	5.5	5.5	15	11	9
Equipment power density (W/m <sup>2</sup> )	4	4	4	20	20	15
Occupancy (person/m <sup>2</sup> )	0.05	0.05	0.05	0.125	0.125	0.125
Cooling/heating setpoints (°C)	26/18	26/18	26/18	26/20	26/20	26/20
Cooling/heating COP	2.7/1.9	2.7/1.9	2.9/2.2	4.2	5.1	5.6

## 2.7. Cool roof modeling

The baseline building models adopt a Typical IEAD (Insulation Entirely Above Deck) Roof structure, which is simplified in this study into three layers: structural substrate, insulation layer, and weather-proof membrane. The structural substrate provides load-bearing capacity while the insulation layer typically composed of rigid foam or mineral fiber, offers continuous thermal resistance to mitigate thermal bridging. The outer protective membrane, usually made of tiles, membranes, or metal panels, ensures waterproofing and durability. The

specific materials used can be found in the referenced report, and the resulting U-values are presented in Table 3. According to the DOE prototype building models, the default solar absorptance of all roofs is set at 0.8, corresponding to a reflectance of 0.2.

In large-scale cool roof retrofits across urban environments, extensive demolition of existing roof assemblies would result in prohibitive costs and operational disruption. Therefore, this study explores three minimally invasive retrofit strategies that require limited structural modification: spray-applied coatings, membrane roofing, and metal roofing, as illustrated in Fig. 9.

Spray coating systems offer a cost-effective solution utilizing liquid-applied reflective materials that adhere directly to existing roof substrates. Membrane roofing enhances durability by incorporating pre-manufactured sheets with superior waterproofing and solar reflectance properties. Although metal roofing systems involve more complex installation procedures, they provide excellent longevity and thermal performance with minimal additional structural loading. The materials and associated costs for each retrofit strategy are presented in Table 4.

To systematically evaluate the impact of cool roof retrofits on energy consumption and economic viability, this study establishes a structured

**Table 4**  
Cool roof retrofit parameters settings.

Parameter	Unit	Baseline	Spray	Membrane	Metal
Investment	RMB/m <sup>2</sup>	—	80	170	350
Maintain time	Year	—	5	15	30
Maintain cost	RMB/m <sup>2</sup>	—	40	20	10
Thickness	mm	0.37	0.5	1.2	0.5
Conductivity	W/m-K	1.1	0.1	1.1	312
Density	kg/m <sup>3</sup>	70	1100	70	479
Specific Heat	J/kg-K	349	1000	1194	349
Solar Absorptance	—	0.8	0.2	0.25	0.37
Thermal Absorptance	—	0.9	0.9	0.75	0.75
Visible Absorptance	—	0.7	0.2	0.6	0.7
Roughness	—	Very Rough	Medium Rough	Smooth	Medium Smooth



**Fig. 9.** Baseline roof and cool roof retrofit scenarios.



framework of Key Performance Indicators (KPIs). The Energy Saving Percentage (ESP) quantifies retrofit performance by comparing the Energy Use Intensity (EUI) of baseline and post-retrofit models, as formalized in Eq. (3):

$$ESP = \frac{EUI_{\text{baseline}} - EUI_{\text{retrofit}}}{EUI_{\text{baseline}}} \times 100\% \quad (3)$$

The Payback Period (PBP) quantifies the time required for an investment to generate cash flows sufficient to recover its initial cost. This metric is widely used in capital budgeting due to its simplicity and intuitive risk assessment capabilities. The formula for calculating PBP can be expressed as follows in Eq. (4)

$$PBP = \frac{\text{Initial Investment}}{\text{Annual Cash Inflow}} \quad (4)$$

Net Present Value (NPV) quantifies the economic viability of an investment by calculating the difference between the present value of discounted cash inflows and outflows over its lifecycle, to assess the profitability of an investment. The NPV calculation is as shown in Eq. (5):

$$NPV = \sum_{t=0}^n \frac{R_t}{(1+r)^t} \quad (5)$$

where  $R_t$  is the net cash inflow at the time  $t$ ,  $r$  is the discount rate, and  $n$  is the remaining life of the building. In China, the life span of residential buildings is usually 50 years. The remaining life span of residential buildings built before 2001, 2001–2010, and built after 2010 is assumed to be 20 years, 30 years, and 40 years.

### 3. Results

Following the methods and modeling process described above, the primary result is a comprehensive building database for Xiamen city. This database encompasses 37,132 individual buildings, with each entry containing detailed information as specified in Table 5. All subsequent results presented in this study are derived from this database.

#### 3.1. The building parameters distribution of Xiamen

Fig. 10 illustrates the distribution of building types and year built in Xiamen. As depicted, residential buildings constitute the predominant category, accounting for 60.8 % of the total. This prevalence is closely linked to Xiamen's rapid urbanization process as a major residential city and Special Economic Zone. Within the residential category, low-rise (32.6 %) and mid-to-high-rise (22.4 %) buildings are the primary subtypes, reflecting urban development patterns and housing demands from

different eras. Mixed-use buildings rank second at 16.7 %, emphasizing functional diversity in Xiamen's urban planning, particularly evident in developments combining residential and commercial uses across various building heights. Commercial buildings represent 11.4 % of the stock, with shopping centers being the principal type, underscoring Xiamen's function as a regional consumption hub.

Regarding building year attributes, it is noteworthy that a substantial majority of buildings (59.4 %) were erected prior to 2002. This high proportion of older stock is likely linked to Xiamen's early designation as a Special Economic Zone in 1980 and the ensuing rapid development phase, consistent with the broader trend of accelerated urbanization and construction in China beginning in the 1980s. This initial period of urban growth established a large foundational building inventory. Furthermore, a distinct peak in construction activity (representing 11.5 % of the stock) is observed around 2009. This surge potentially correlates with national economic stimulus policies implemented in China at the time, coupled with the rapid expansion of Xiamen's local real estate market.

#### 3.2. The building roof distribution

Fig. 11 illustrates the spatial distribution of rooftop colors on Xiamen, derived from standardized 100 m × 100 m grid-based analysis. As shown in Fig. 11(a), the spatial heterogeneity of rooftop colors reveals distinct patterns across different urban zones. These data are based on rooftop color statistics extracted from remote sensing imagery. Fig. 11(b) presents the detailed extraction for individual buildings, demonstrating that the employed image processing methodology involving multispectral image fusion and color correction successfully captures the main color characteristics of building rooftops. The accuracy of this extraction facilitates a reliable representation of urban rooftop hues. In Fig. 11(c), the color composition histogram further indicates that light-colored rooftops dominate the urban fabric, while red-toned roofing materials also occupy a considerable proportion. Such a distribution pattern reflects a dual strategy in urban planning: on the one hand, light-colored and higher-albedo rooftops are widely adopted in newly developed districts to improve thermal performance and reduce cooling energy loads, and the controlled presence of red-toned rooftops supports the preservation of the city's architectural identity and visual coherence.

Fig. 12 presents the analysis results of rooftop reflectance within the study area of Xiamen. Fig. 12(a) displays the spatial distribution of rooftop reflectance values, which range from 0 to 0.46. In this map, darker shades correspond to lower reflectance values, while lighter shades indicate higher reflectance. Fig. 12(b) shows representative rooftop imagery paired with annotated reflectance values, illustrating how different materials and surface colors influence reflectance characteristics. Fig. 12(c) provides a histogram that statistically summarizes rooftop reflectance across the entire study region. The results indicate that most rooftops have reflectance values concentrated around 0.25, and the overall distribution approximates a normal curve. This suggests that a majority of rooftops in Xiamen exhibit low to moderate solar reflectance. From an urban energy perspective, such reflectance levels imply opportunities for energy efficiency improvement through the adoption of cool roof technologies, which typically feature reflectance values above 0.7.

#### 3.3. The UBE M result

##### 3.3.1. Baseline

Fig. 13 presents the simulated distribution of energy use intensity (EUI) for 31,608 buildings in 37,132 buildings in Xiamen, a representative city in the hot summer and warm winter climate zone. The simulation integrates three key influencing factors: building year (which primarily affects the thermal performance of the building envelope), surrounding shadings, and roof solar reflectance. The analysis reveals that electricity EUI primarily associated with cooling demand and

**Table 5**  
Main parameters of Xiamen building database.

Name	Data Type	Description
Geometry	Polygon	2D coordinates defining the building footprint
Type	String	Building category (e.g., Residential, Commercial)
Year Detail	Number	Specific building year (e.g., 2010)
Year	String	Year range or textual description (e.g., "Pre-2000")
R,G,B	Numbers	RGB color values (0–255) for Roof (e.g., "255,0,0" for red)
Reflection	Number	Roof reflectivity coefficient (0–1)
Height	Number	Vertical height of the building in meters
Number Of Stories	Number	Total count of stories
Gas EUI	Number	Gas Energy Use Intensity (kWh/m <sup>2</sup> /year)
Electricity EUI	Number	Electricity Energy Use Intensity (kWh/m <sup>2</sup> /year)
Gas Total	Number	Annual total gas consumption in kilowatt-hours (kWh)
Electricity Total	Number	Annual total electricity consumption in kilowatt-hours (kWh)

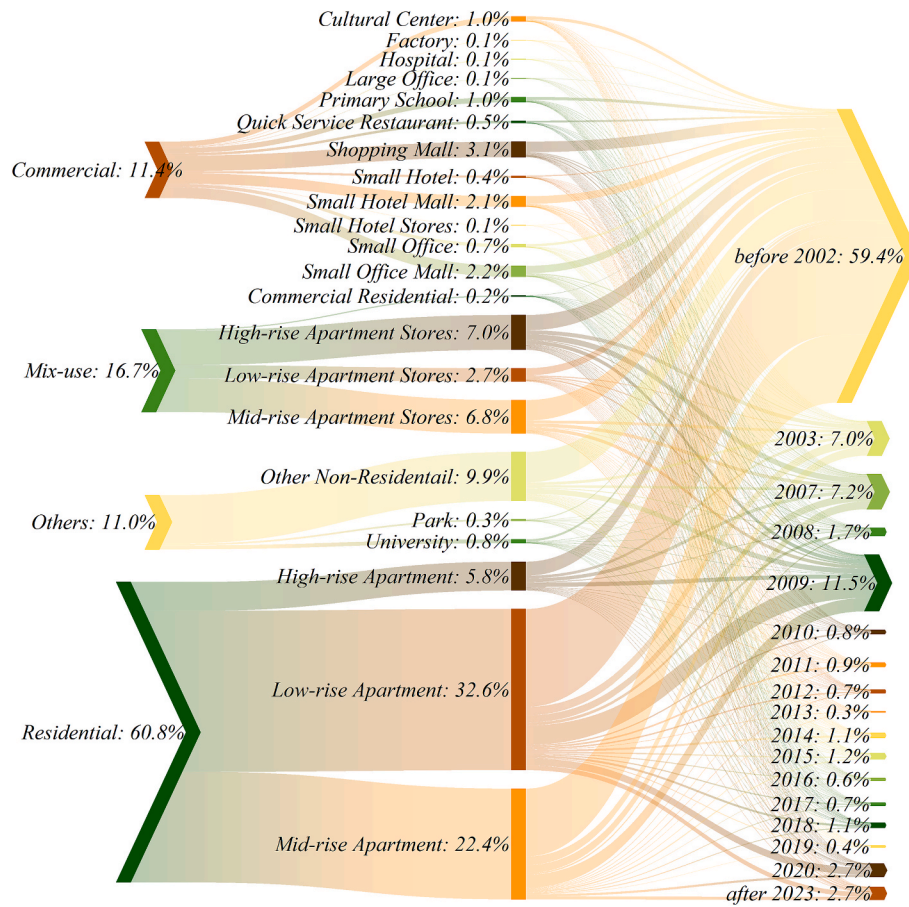


Fig. 10. Results of building types and ages on Xiamen.

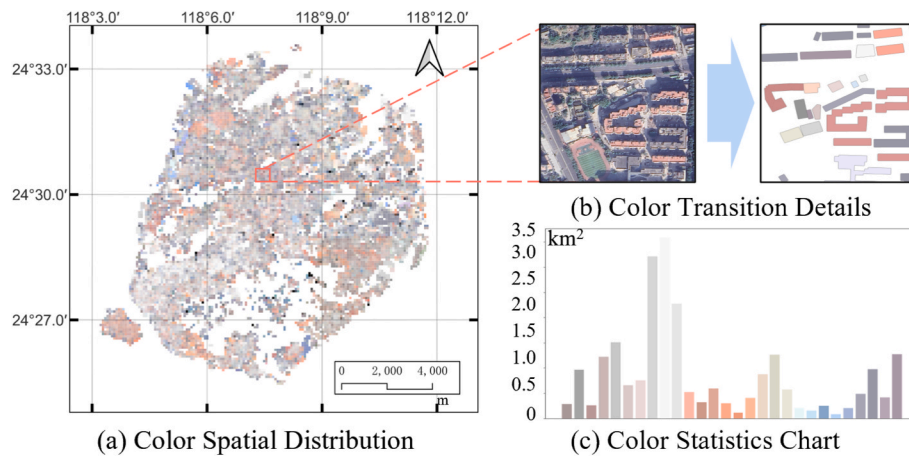


Fig. 11. Distribution of roof colors in Xiamen.

represented by the blue/cyan distribution exhibits a wide range and multimodal pattern, indicating the heterogeneity in building energy efficiency across the city. In contrast, the natural gas EUJ mainly used for domestic hot water and shown in red/orange remains consistently low and narrowly distributed, suggesting its limited sensitivity to envelope characteristics and solar heat gains.

The categories shown in Fig. 13 each exhibit three major peaks, reflecting the classification of buildings into three building-year groups. Beyond these peaks, the distributions also display quasi-normal characteristics, which closely resemble the distribution pattern of roof reflectance. However, these distributions are not strictly normal,

primarily due to the influence of surrounding shading buildings, which modulates solar heat gains and thermal transfer, thereby affecting cooling loads. Given that cooling demand far exceeds heating needs in Xiamen's climatic context, the control of solar heat gains is a critical factor in building energy conservation. The simulation explicitly incorporates roof reflectance and shadings as input variables, enabling its outcomes to go beyond traditional assessments based solely on building year or single-envelope parameters. As a result, it more accurately captures the real-world impact of surface properties on energy use in buildings. This indicates that the simulation framework is capable of directly evaluating the energy-saving potential of high-reflectance

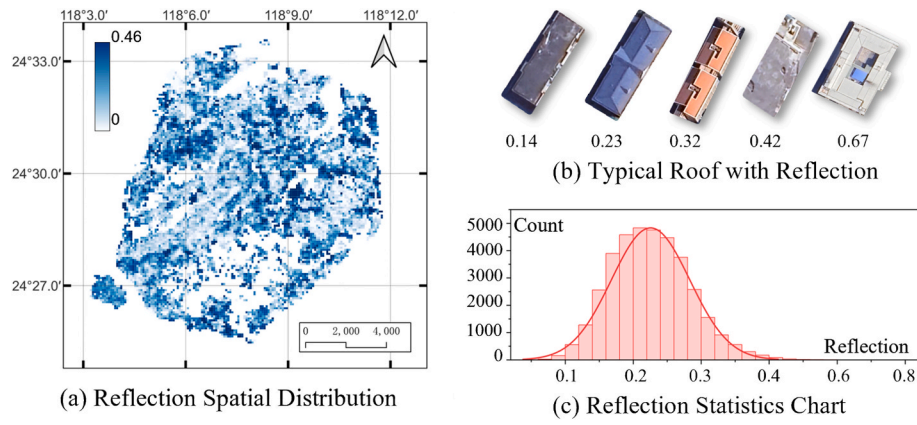


Fig. 12. Distribution of roof reflection in Xiamen.

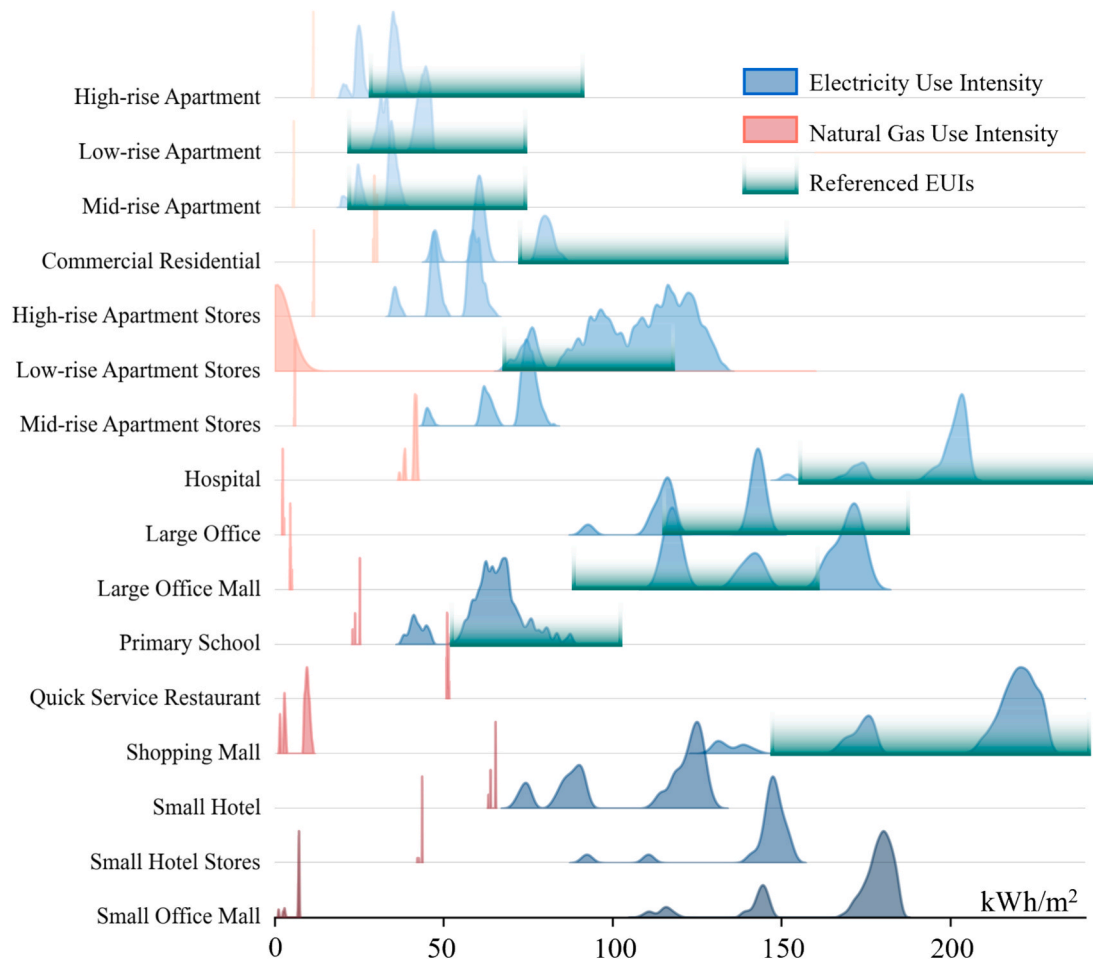


Fig. 13. Energy demand distribution across typical building types in Xiamen.

technologies, such as cool roofs. By systematically adjusting the roof reflectance parameter in the simulation, it is possible to quantitatively predict the contribution of cool roof implementation particularly for high electricity-EUI building groups to energy consumption reduction, as well as its influence on the overall shape of the EUI distribution curve.

Fig. 14 illustrates the spatial differentiation of building energy consumption within the built-up area of Xiamen. The analysis of electricity consumption reveals significant spatial heterogeneity and clustering, with high-intensity electricity use concentrated in the central and southern parts of the island areas corresponding to the city's core

functional zones. The highest consumption in a single grid cell reaches 59.4 GWh, largely reflecting the heavy dependence on electricity in commercial centers, high-density residential areas, and specific industrial activities. In contrast, although natural gas consumption also shows localized concentrations, it demonstrates a more extensive spatial coverage overall. Its peak consumption intensity (13.6 GWh) is substantially lower than that of electricity, suggesting that natural gas is primarily used for residential purposes such as cooking and domestic hot water. As a result, its spatial distribution aligns more closely with the layout of residential neighborhoods.



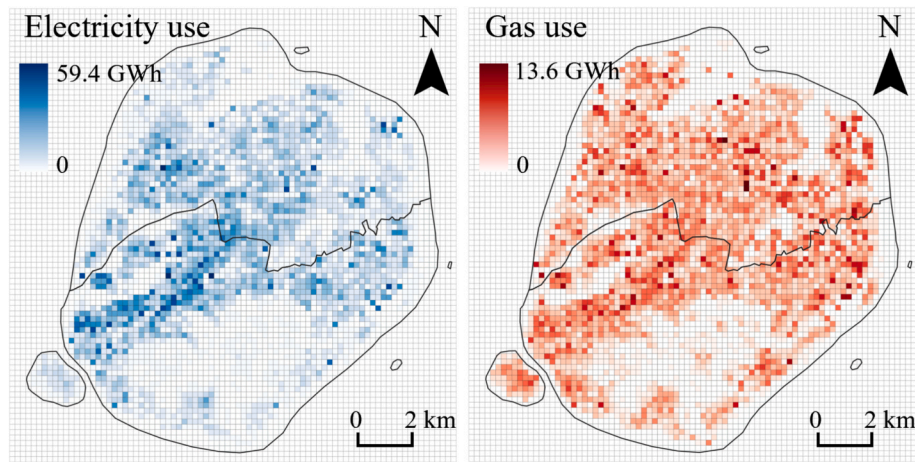


Fig. 14. Spatial patterns of electricity and gas use in Xiamen.

### 3.3.2. Cool roof application

As shown in the Fig. 15, this study evaluates the effectiveness of different cool roof retrofit strategies in Xiamen, with a particular focus on the influence of roof surface properties. The “Predicted” scenario refers to results derived from measured roof reflectance values of actual buildings. Compared to the Baseline, the Predicted scenario demonstrates improved energy performance, indicating that the use of default reflectance values tends to overestimate building energy consumption. Among the cool roof technologies evaluated, metal, membrane, and spray-applied systems reduce total energy use by 1.19 GWh, 1.88 GWh, and 2.32 GWh, respectively corresponding to energy savings of 2.27 %, 3.58 %, and 4.42 %. These reductions are primarily attributable to decreased cooling demand, aligning with the theoretical expectation that cool roofs reduce indoor heat gain by increasing solar reflectance and lowering roof surface temperature. It is worth noting that heating energy consumption shows a slight increase under cool roof scenarios. However, given Xiamen’s hot summer and warm winter climate, this increase is marginal and significantly outweighed by the reduction in cooling energy use.

Fig. 16 illustrates the cooling demand curves on July 21st, the typical summer day for buildings on Xiamen. Using the Predicted scenario as a reference, Fig. 16 shows that the Spray scenario consistently exhibits the lowest cooling energy consumption, while the Predicted scenario

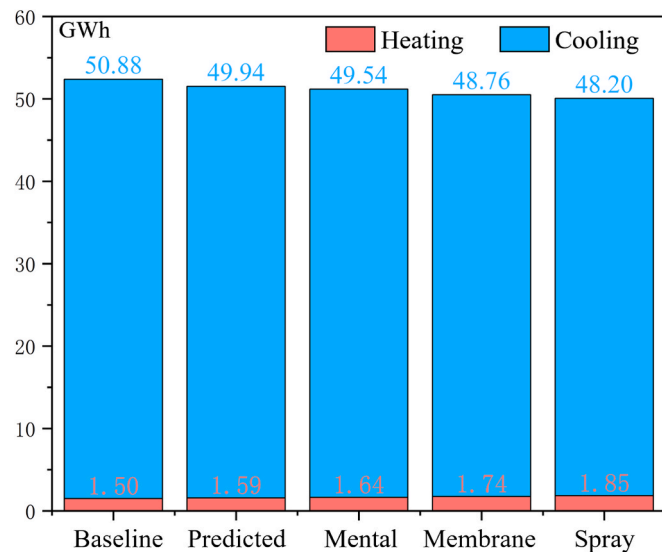


Fig. 15. Total heating and cooling energy consumption under different cool roofs.

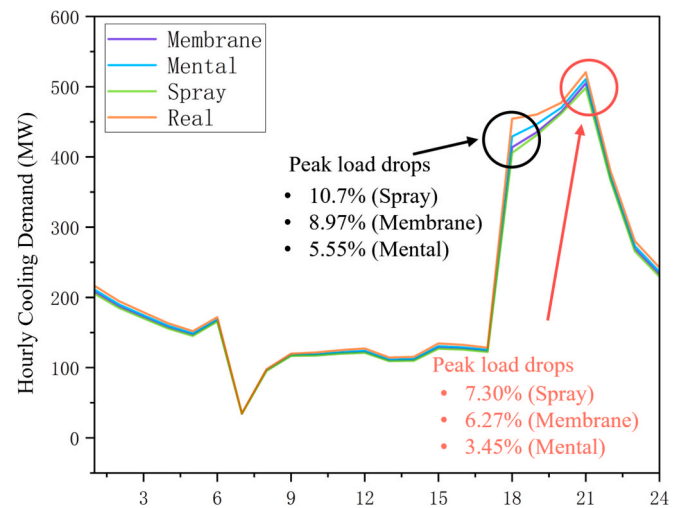


Fig. 16. Peak load reduction effects of cool roof strategies on July 21st in Xiamen.

remains at the higher end.

During the early morning hours, cooling demand reaches its lowest level of the day, reflecting reduced building occupancy and lower ambient temperatures at night. As economic activities begin and solar radiation intensifies, cooling loads gradually increase, reaching a relatively stable plateau or forming a secondary peak in the early afternoon (approximately 13:00 to 15:00). Subsequently, during the evening hours (approximately 18:00 to 21:00), cooling demand rises sharply, reaching its daily maximum. This evening peak significantly exceeds the daytime levels and is primarily attributed to the large number of residential buildings, where returning occupants generate a surge in cooling demand. Notably, peak values are observed at both 18:00 and 21:00. However, the peak-shaving effect of cool roof technologies is more pronounced at 18:00, achieving reductions of 10.7 %, 8.97 %, and 5.5 % for the Spray, Membrane, and Metal scenarios, respectively. This enhanced performance is due to the continued presence of solar radiation during this period, making the reflectance-based cooling effect of cool roofs more effective.

Overall, Fig. 16 demonstrates the potential of cool roof technologies to reduce urban peak loads and provides a valuable analytical basis for optimizing energy dispatch and demand-side management strategies.

Three types of cool roof retrofitting methods, including spray coating, membrane, and metal were selected for evaluation, along with a corresponding economic assessment. Among the 31,608 buildings



where energy consumption simulation was feasible, 3790 buildings (approximately 12 %) were found to meet the economic feasibility criterion of a PBP of less than 10 years. Of these, 1298 buildings were more suitable for membrane retrofitting, 2492 for spray coating, while none were identified as suitable for metal retrofitting due to its excessively high initial investment cost.

Over the analysis period extending to the year 2070, the total initial investment for economically feasible retrofits was estimated at 35.3 million CNY (approximately 4.8 million USD), with maintenance costs amounting to approximately 39.3 million CNY (5.3 million USD), resulting in a total life-cycle cost of 10.19 million CNY. Throughout their life cycles, these buildings achieved electricity savings of 151.67 GWh and a corresponding increase in natural gas consumption of 2.39 GWh. Based on an electricity rate of 0.6 CNY/kWh, the overall energy cost savings were estimated at approximately 89.6 million CNY, resulting in a net economic benefit of around 15.0 million CNY (2.0 million USD) over the building lifespans.

Further analysis, as shown in Fig. 17, indicates that in the context of Xiamen, both building type and the number of floors significantly affect the most suitable retrofitting method, while the building year appears to have a relatively minor influence. Nevertheless, older buildings tend to exhibit higher economic retrofitting potential. Newly constructed buildings, due to improved envelope performance, generally offer lower energy-saving potential, thereby demonstrating a decreasing trend in retrofit benefits.

In terms of building height, spray coating was found to be more advantageous in both low-rise and high-rise buildings (above 30 floors). This can be attributed to the relatively larger roof-to-volume ratio in low-rise buildings, where rooftop heat gain substantially affects energy consumption. In such cases, spray coating provides sufficient energy savings to achieve payback within 10 years, while also presenting lower life-cycle costs due to reduced maintenance frequency and expense. For mid-rise buildings, membrane retrofitting showed greater economic viability, likely due to its lower maintenance cost per cycle, extended performance lifespan, or improved cumulative energy-saving effect, which leads to greater net benefits.

With respect to building type, spray coating was generally found to be more suitable for residential buildings. This may be attributed to the

typically lower Energy Use Intensity (EUI) of residential structures, making the low installation cost of spray coating more favorable. On the other hand, membrane retrofitting was identified as more appropriate for fast-food restaurants, large shopping malls, and other commercial buildings. These buildings are often characterized by daytime operation, substantial internal heat gains, and high cooling demands. In such scenarios, the lower maintenance costs and higher cumulative energy-saving value of membrane systems contribute to a faster return on investment within the 10-year evaluation period.

#### 4. Discussion

Cool roofs have recently attracted increasing attention as a building energy efficiency technology, primarily involving the enhancement of roof surface reflectance. However, many of these studies rely on assumed or default roof reflectance values, which can significantly overestimate the energy-saving potential of cool roof applications. At the urban scale, a more accurate assessment requires actual reflectance data from existing roofs. Obtaining such data is a critical challenge in large-scale urban building energy modeling, particularly in less developed regions where open-access building information is limited or nonexistent. Various researchers have attempted to address this gap by supplementing missing building information, such as footprint, height, type, age, and window-to-wall ratio, through diverse data sources and inference techniques. These data enhancements improve the realism of urban energy models, enabling more accurate quantification of the large-scale impacts of building technologies and supporting better-informed policy decisions.

This study presents a comprehensive case study of cool roof application in Xiamen. It details the full pipeline from data acquisition and preprocessing to urban-scale building energy simulation based on an integrated dataset of the entire island's building stock. A city-level building database for Xiamen was developed, incorporating key information such as building year and type. This study proposes a method for estimating building year, which performs well even in fully built-up areas while significantly reducing computational cost and improving accuracy. In addition, the study expands the range of urban building data sources by integrating platforms such as Google Earth Engine and very high-resolution imagery. These sources enabled the inclusion of surface features such as roof color and reflectance into the database. To the best of our knowledge, this study presents the first city-scale evaluation of cool roof applications based on actual rooftop reflectance data. Although green roofs are often discussed alongside cool roofs, as noted by He et al. [5], the cooling mechanisms of green roofs are more complex, as they involve evapotranspiration, shading, thermal insulation, and thermal mass. This complexity also poses challenges for modeling. Therefore, this study did not include modeling and comparison of green roofs but instead focused on extending the applicability of cool roofs using new data sources.

This study has several limitations. First, the analysis is limited to the central area of Xiamen, rather than the entire city. This may underestimate the average energy-saving potential of cool roofs, as non-central areas may feature lower building heights and therefore benefit more. Second, global warming is an ongoing reality. In the face of future climate change, the widespread adoption of rooftop retrofits such as cool roofs and green roofs may influence the urban microclimate [31], this cooling effect could further enhance the energy-saving performance of cool roofs and improve urban thermal comfort. However, this study does not account for such potential feedback effects, representing a limitation in the current analysis. Thirdly, obtaining city-scale measured energy consumption data remains a significant challenge, and as such, the model was not calibrated with measured data. Nevertheless, to maximize model accuracy, this study customized building parameters based on Xiamen's local standards, employed the widely recognized EnergyPlus simulation engine, and benchmarked prototype buildings against measured or reported energy consumption data from similar regional

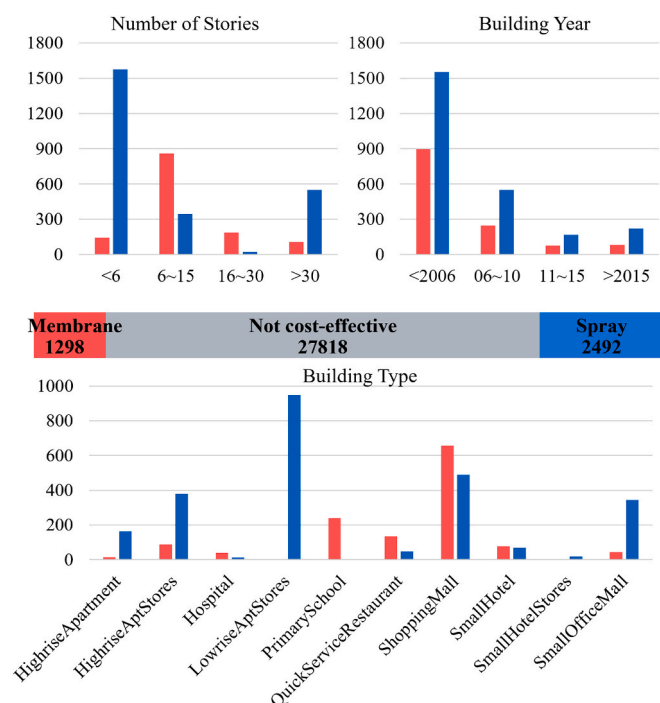


Fig. 17. Distribution of Building attributes for different cool roof retrofit.

buildings.

## 5. Conclusions

This study developed and applied a high-resolution UBEM framework, integrating actual roof reflectance data derived from multi-source satellite imagery, to comprehensively evaluate the energy-saving potential and economic feasibility of cool roof retrofits at the city scale for Xiamen, China. The key findings and contributions are summarized as follows:

- **Quantification of Actual Reflectance Impact:** A detailed geospatial dataset for 37,132 buildings was created, incorporating building type, building year, and actual roof reflectance derived from Sentinel-2 and VHR imagery. Utilizing these measured reflectance values in the UBEM simulation for 31,608 buildings revealed a city-wide energy consumption reduction of 1.8 % (0.94 GWh) compared to simulations using the commonly assumed default reflectance of 0.2.
- **Performance Assessment of Cool Roof Technologies:** Three distinct cool roof technologies were evaluated. Spray coatings demonstrated the highest annual energy savings potential at 4.42 % (2.32 GWh), followed by membranes roofs (3.58 %, 1.88 GWh) and metal (2.27 %, 1.19 GWh). Correspondingly, these technologies achieved significant peak cooling load reductions on a typical summer day, estimated at 10.7 %, 5.5 %, and 8.97 %, respectively.
- **Economic Viability and Implementation Strategy:** An economic analysis identified 3790 buildings as economically viable for cool roof retrofitting, defined by a payback period of less than 10 years. Among these, spray coatings were suitable for 2492 buildings and membranes for 1298 buildings. The life-cycle assessment for these feasible retrofits projected net savings of approximately 15.0 million CNY, resulting from 151.67 GWh of electricity savings against an initial investment of 35.3 million CNY and maintenance costs of 39.3 million CNY.

In conclusion, this study provides a city-scale assessment of cool roof potential in Xiamen based on actual rooftop conditions, offering crucial quantitative insights into energy savings, peak load reduction, and economic feasibility. The findings and the developed UBEM framework serve as a valuable reference for policymakers and urban planners in formulating targeted energy efficiency strategies and promoting sustainable building retrofitting programs, particularly for Xiamen and other cities with similar climatic conditions and urban characteristics.

## CRedit authorship contribution statement

**Chengcheng Song:** Writing – review & editing, Writing – original draft, Validation, Software, Methodology, Data curation, Conceptualization. **Yixing Chen:** Writing – review & editing, Supervision, Funding acquisition, Conceptualization.

## Declaration of competing interest

The authors declare that they have no known competing financial interests or personal relationships that could have appeared to influence the work reported in this paper.

## Acknowledgments

This paper is supported by the National Natural Science Foundation of China (NSFC) through Grant No. 52478088. This paper is also funded by the Key Research and Development Project of Hunan Province of China through Grant No. 2024AQ2011.

*Declaration of Generative AI and AI-assisted technologies in the writing process.*

During the preparation of this work, the authors used Grammarly and ChatGPT to improve readability and detect spelling/grammar mistakes. After using these tools/services, the authors reviewed and edited the content as needed and take full responsibility for the content of the publication.

## Data availability

Data will be made available on request.

## References

- [1] J. Chen, Lu. Lin, Comprehensive evaluation of thermal and energy performance of radiative roof cooling in buildings, *J. Build. Eng.* 33 (2021) 101631, <https://doi.org/10.1016/j.jobe.2020.101631>.
- [2] Y. Gao, D. Shi, R. Levinson, R. Guo, C. Lin, J. Ge, Thermal performance and energy savings of white and sedum-tray garden roof: a case study in a Chongqing office building, *Energy Buildings* 156 (2017) 343–359, <https://doi.org/10.1016/j.enbuild.2017.09.091>.
- [3] J. Dong, M. Lin, J. Zuo, T. Lin, J. Liu, C. Sun, J. Luo, Quantitative study on the cooling effect of green roofs in a high-density urban area—A case study of Xiamen, China, *J. Clean. Prod.* 255 (2020) 120152, <https://doi.org/10.1016/j.jclepro.2020.120152>.
- [4] S. Jia, Q. Weng, C. Yoo, H. Xiao, Q. Zhong, Building energy savings by green roofs and cool roofs in current and future climates, *Npj Urban Sustain.* 4 (1) (2024) 23, <https://doi.org/10.1038/s42949-024-00159-8>.
- [5] Y. He, Yu. Hang, A. Ozaki, N. Dong, Thermal and energy performance of green roof and cool roof: a comparison study in Shanghai area, *J. Clean. Prod.* 267 (2020) 122205, <https://doi.org/10.1016/j.jclepro.2020.122205>.
- [6] C.F. Reinhart, C.C. Davila, Urban building energy modeling – a review of a nascent field, *Build. Environ.* 97 (2016) 196–202, <https://doi.org/10.1016/j.buildenv.2015.12.001>.
- [7] T. Hong, Y. Chen, X. Luo, Na. Luo, S.H. Lee, Ten questions on urban building energy modeling, *Build. Environ.* 168 (2020) 106508, <https://doi.org/10.1016/j.buildenv.2019.106508>.
- [8] Y.Q. Ang, Z.M. Berzolla, C.F. Reinhart, From concept to application: a review of use cases in urban building energy modeling, *Appl. Energy* 279 (2020), <https://doi.org/10.1016/j.apenergy.2020.115738>.
- [9] L. Shu, Y. Mo, D. Zhao, Energy retrofits for smart and connected communities: scopes and technologies, *Renew. Sustain. Energy Rev.* 199 (2024) 114510, <https://doi.org/10.1016/j.rser.2024.114510>.
- [10] U. Ali, M.H. Shamsi, C. Hoare, E. Mangina, J. O'Donnell, Review of urban building energy modeling (UBEM) approaches, methods and tools using qualitative and quantitative analysis, *Energ. Buildings* 246 (2021) 111073, <https://doi.org/10.1016/j.enbuild.2021.111073>.
- [11] C. Wang, M. Ferrando, F. Causone, X. Jin, X. Zhou, X. Shi, Data acquisition for urban building energy modeling: a review, *Build. Environ.* 217 (2022) 109056, <https://doi.org/10.1016/j.buildenv.2022.109056>.
- [12] Z. Deng, Y. Chen, X. Pan, Z. Peng, J. Yang, Integrating GIS-based point of interest and community boundary datasets for urban building energy modeling, *Energies* 14 (4) (2021) 1049, <https://doi.org/10.3390/en14041049>.
- [13] C. Song, Z. Deng, W. Zhao, Y. Yuan, M. Liu, Xu. Shen, Y. Chen, Developing urban building energy models for Shanghai City with multi-source open data, *Sustain. Cities Soc.* 106 (2024) 105425, <https://doi.org/10.1016/j.scs.2024.105425>.
- [14] Z. Sun, Y. Gao, J. Yang, Y. Chen, B.H.W. Guo, Development of urban building energy models for Wellington city in New Zealand with detailed survey data on envelope thermal characteristics, *Energ. Buildings* 321 (2024) 114647, <https://doi.org/10.1016/j.enbuild.2024.114647>.
- [15] F. Biljecki, M. Sindram, 2017. 'ESTIMATING BUILDING AGE WITH 3D GIS'. *ISPRS Annals of the Photogrammetry, Remote Sensing and Spatial Information Sciences* IV-4/W5:17–24. doi:10.5194/isprs-annals-IV-4-W5-17-2017.
- [16] C. Wang, S. Wei, S.H. Du, D. Zhuang, Y.X. Li, X. Shi, X. Jin, X. Zhou, A systematic method to develop three dimensional geometry models of buildings for urban building energy modeling, *Sustain. Cities Soc.* 71 (2021), <https://doi.org/10.1016/j.scs.2021.102998>.
- [17] W. Chen, Y. Zhou, Q. Wu, G. Chen, B. Yu, Urban building type mapping using geospatial data: a case study of Beijing, China, *Remote Sens. (Basel)* 12 (17) (2020) 2805, <https://doi.org/10.3390/rs12172805>.
- [18] Z. Lu, Building type classification using spatial and landscape attributes derived from LiDAR remote sensing data, *Landsc. Urban Plan.* (2014), <https://doi.org/10.1016/j.landurbplan.2014.07.005>.
- [19] J.T. Szcześniak, Y.Q. Ang, S. Letellier-Duchesne, C.F. Reinhart, A method for using street view imagery to auto-extract window-to-wall ratios and its relevance for urban-level daylighting and energy simulations, *Build. Environ.* 207 (2022), <https://doi.org/10.1016/j.buildenv.2021.108108>.
- [20] D. Dilsiz, K.N. Aysegul, J. Kämpf, Z. Nagy, Ranking parameters in urban energy models for various building forms and climates using sensitivity analysis, *Build. Simul.* (2022), <https://doi.org/10.1007/s12273-022-0961-5>.

- [21] M. Wang, Yu. Hang, Y. Liu, J. Lin, X. Zhong, Y. Tang, H. Guo, R. Jing, Unlock city-scale energy saving and peak load shaving potential of green roofs by GIS-informed urban building energy modelling, *Appl. Energy* 366 (2024) 123315, <https://doi.org/10.1016/j.apenergy.2024.123315>.
- [22] I. Adilkhanova, M. Santamouris, G.Y. Yun, Green roofs save energy in cities and fight regional climate change, *Nat. Cities* 1 (3) (2024) 238–249, <https://doi.org/10.1038/s44284-024-00035-7>.
- [23] M. Hosseini, H. Akbari, Effect of cool roofs on commercial buildings energy use in cold climates, *Energ. Buildings* 114 (2016) 143–155, <https://doi.org/10.1016/j.enbuild.2015.05.050>.
- [24] S. Garshasbi, J. Feng, R. Paolini, J.J. Duverge, C. Bartesaghi-Koc, S. Arasteh, A. Khan, M. Santamouris, On the energy impact of cool roofs in Australia, *Energ. Buildings* 278 (2023) 112577, <https://doi.org/10.1016/j.enbuild.2022.112577>.
- [25] V. Lalwani, A. Sobti, V. Garg, What's up on the roof: tracking cool roofs in india with satellite imaging, *ACM J. Comput. Sustain. Soc.* (2024) 3685696, <https://doi.org/10.1145/3685696>.
- [26] J. Park, S. Park, J. Kang, Detecting and classifying rooftops with a CNN-based remote-sensing method for urban area cool roof application, *Energy Rep.* 11 (2024) 2516–2525, <https://doi.org/10.1016/j.egy.2024.02.001>.
- [27] Z. Qian, M. Chen, Z. Sun, F. Zhang, Xu. Qingsong, J. Guo, Z. Xie, Z. Zhang, Simultaneous extraction of spatial and attributional building information across large-scale urban landscapes from high-resolution satellite imagery, *Sustain. Cities Soc.* 106 (2024) 105393, <https://doi.org/10.1016/j.scs.2024.105393>.
- [28] F. Trevisiol, A. Lambertini, F. Franci, E. Mandanici, An object-oriented approach to the classification of roofing materials using very high-resolution satellite stereo-pairs, *Remote Sens. (Basel)* 14 (4) (2022) 849, <https://doi.org/10.3390/rs14040849>.
- [29] S. Bonafoni, A. Sekertekin, Albedo retrieval from Sentinel-2 by new narrow-to-broadband conversion coefficients, *IEEE Geosci. Remote Sens. Lett.* 17 (9) (2020) 1618–1622, <https://doi.org/10.1109/LGRS.2020.2967085>.
- [30] C. Song, J. Yang, Z. Wang, R. Li, X. Pang, Y. Chen, CityEL: a web-based platform to support city-scale building energy efficiency based on AutoBPS, *Sustain. Cities Soc.* 120 (2025) 106147, <https://doi.org/10.1016/j.scs.2025.106147>.
- [31] Y. He, E.S. Lin, W. Zhang, C.L. Tan, P.Y. Tan, N.H. Wong, Local microclimate above shrub and grass in tropical city: a case study in Singapore, *Urban Clim.* 43 (2022) 101142, <https://doi.org/10.1016/j.uclim.2022.101142>.